crystals

MDPI

Article

Performance of Pico-Second Laser-Designed Silicon/Gold Composite Nanoparticles Affected by Precision of Focus Position

Yury V. Ryabchikov [1,*], Antonin Kana [2] and Inam Mirza [1]

[1] HiLASE Centre, FZU—Institute of Physics of the Czech Academy of Sciences, Scientific Laser Applications Department, Za Radnicí 828, 252 41 Dolní Břežany, Czech Republic
[2] Department of Analytical Chemistry, University of Chemistry and Technology, Prague Technická 5, 166 28 Prague, Czech Republic; antonin.kana@vscht.cz
* Correspondence: yury.ryabchikov@hilase.cz

Abstract: Pulsed laser ablation in liquids is one of the most versatile and widespread techniques for the easy synthesis of different types of nanoparticles with controllable properties. A huge amount of energy compressed into one pulse that is directed onto a solid target leads to the ejection of materials into surrounding liquid. However, the precision of the focus of laser irradiation can play a crucial role in the synthesis of nanomaterials and, hence, significantly affect their physico-chemical properties. In this paper, we investigated the influence of the focus position of the laser spot on the optical properties of single- and double-element composite silicon/gold nanoparticles, as well as on their structure and chemical composition. Deepening of the focus to 0.5 mm inside the bulk material led to better chemical stability of the colloidal solutions and increased the particle and mass concentrations of the generated nanoparticles. This larger amount of materials led to a stronger absorbance, and resulted in slightly better photoluminescence excitation efficiencies for all nanostructures. Silicon-based nanoparticles had a remarkable photoluminescence peak at ~430 nm upon xenon lamp excitation, which was the most pronounced for pure silicon nanoparticles synthesized at the F+0.5 focus position. This position also led to the best laser-induced heating (~0.85 °C/min) of the colloidal solutions. All nanocomposites revealed amorphous silicon structures with some Si(111) and Au(111), suggesting the formation of gold silicide with different stoichiometries. The observed findings can help in choosing appropriate experimental conditions to achieve the best performance of laser-synthesized colloidal solutions of composite silicon/gold nanostructures.

Keywords: pulsed laser ablation; silicon/gold nanoparticles; composite nanoparticles; laser-induced heating; focus precision

check for updates

Academic Editors: John Parthenios and Leonid Kustov

Received: 27 November 2024
Revised: 21 December 2024
Accepted: 15 January 2025
Published: 25 January 2025

Citation: Ryabchikov, Y.V.; Kana, A.; Mirza, I. Performance of Pico-Second Laser-Designed Silicon/Gold Composite Nanoparticles Affected by Precision of Focus Position. *Crystals* **2025**, *15*, 132. https://doi.org/10.3390/cryst15020132

Copyright: © 2025 by the authors. Licensee MDPI, Basel, Switzerland. This article is an open access article distributed under the terms and conditions of the Creative Commons Attribution (CC BY) license (https://creativecommons.org/licenses/by/4.0/).

1. Introduction

Pulsed laser ablation in liquids (PLAL) is one of the easiest and most prominent techniques for synthesizing nanostructures from any chemical element. The compression of all laser energy into a pulse with a very short duration (ps or fs) results in the concentration of a huge amount of energy in a small laser spot. Such laser fluence can destroy the surface of a target immersed in a liquid medium. This laser–matter interaction leads to the release of nanoclusters, which are confined by the surrounding liquid medium. Comprehensive information considering diverse targets and organic/inorganic liquids is summarized in the following reviews [1,2]. Further interaction between different nanoclusters leads to the creation of nanoparticles (NPs) with physico-chemical properties that are strongly affected

by numerous experimental conditions (e.g., wavelength, pulse duration, laser fluence, treatment duration, used liquid, etc.) [3,4].

Usually, laser ablation efficiency increases with longer laser irradiation wavelengths (~4.4 mg/h for Pt NPs at 1064 nm), also resulting in a higher optical density of the synthesized colloidal solutions [5,6]. This is mainly explained by the higher contribution of self-absorption of the shorter-wavelength irradiation by NPs, which decreases the laser fluence on the target surface [6,7]. It is worth noting that for shorter wavelengths, the ablation efficiency is greater at a lower fluence, while for longer wavelengths, it is greater at a higher fluence [8]. Increasing the laser fluence tends to cause a stronger absorbance intensity, suggesting a higher amount of NPs in the surrounding liquid due to larger productivity (~2 μg/s for 1.3 J/cm^2) [6,9,10]. Moreover, it also leads to larger mean sizes of NPs due to the longer lifetime of the cavitation bubbles, affected by greater temperatures and pressures of the laser plume [11–13]. By changing the repetition rate of the laser ablation process, one can also control the ablation efficiency and the productivity of NPs (~350 μg/min at 5000 Hz) [14]. Varying the laser processing time increases the concentration of the produced materials, considerably affecting their structural and optical properties, in both direct laser ablation and fragmentation techniques (~300–400 μg/min at 10 min ablation time) [15–17]. Moreover, the type of laser processing approach used—direct laser ablation or laser co-fragmentation—also considerably affects the size, content, optical properties, and performance of metallic–semiconductor nanocomposites [18].

Additionally, the inorganic and organic substances in the liquid medium used also affect the properties of laser-synthesized nanostructures, depending on the characteristics of these substances. In particular, the concentration of semiconductor NPs dispersed in water strongly affects the mean size and chemical composition of Si/Au nanocomposites, altering their opto-electronic properties [19]. The presence of inorganic precursors (e.g., $HAuCl_4$, $AgNO_3$, etc.) in a liquid results in the formation of composite nanostructures, such as Si/Au or Si/Ag, with efficient light-to-heat transfer modalities [20,21]. Various gold-decorated TiO_2 nanocomposites are also prepared using unfocused or focused laser irradiation, demonstrating prospects in anticancer, SERS, and photothermal conversion activities [22–24].

The liquid used for laser ablation synthesis can also influence the productivity, size, and structural properties of the generated nanostructures. Indeed, ablation in acetone was found to slightly increase the productivity of Al NPs (~0.40 μg/pulse) in comparison with ablation in ethanol (~0.37 μg/pulse), but significantly increased their productivity compared to ethylene glycol (~0.03 μg/pulse) [25]. However, the water-mediated medium had a higher ablation rate than the alcohol-mediated one, due to the lower breakdown thresholds of alcohols [26]. Besides controlling the size of nanoparticles, the liquid used can also affect their chemical composition—in particular, the oxidation of nanostructures [27]. Another important point that is often missed in papers related to the PLAL synthesis of nanoparticles is the precision of the focus position. Indeed, even a slight imprecision in focus can lead to a significant mismatch between the physico-chemical properties of the synthesized nanostructures and their performance in real applications. In particular, modification of the target position with respect to the radiation focus has been found to change plasma formation, correlating with the productivity, size, and optical properties of nanostructures [9,28]. Changing the focus of laser irradiation (1064 nm, 6 ps) was found to considerably affect the productivity of the laser ablation synthesis of silver nanoparticles, which reached 7–9 μg/s, depending on the repetition rate [29]. It was also found to influence the optical density and size distribution of colloidal solutions of plasmonic nanoparticles [30,31]. However, during the synthesis of multi-element NPs, precision of the focus position can be even more crucial. In this case, it will affect not only the ablated

target, but also the dispersed NPs, influencing numerous physico-chemical characteristics of the composite nanostructures. To study the properties of nanocomposites (NCs), the following semiconductor and metallic materials were chosen in this research, due to their numerous biomedical (silicon) and plasmonic sensing (gold) applications [32–35], which can be further significantly improved by the formation of multi-element nanostructures.

In this paper, we study the influence of the position of focus of ps laser irradiation on the optical and structural properties of various synthesized silicon/gold nanoparticles, as well as on the content of different chemical elements. We found that a higher concentration of single- and double-element Si/Au nanoparticles, with a larger hydrodynamic size, were produced at the F + 0.5 focus position. This position of laser irradiation improved the chemical stability of all colloidal solutions in comparison with precise focusing. A larger amount of nanoparticles enhanced the absorbance of the colloidal solutions prepared at this focus position, resulting in slightly better photoluminescence excitation (PLE) efficiency. All silicon-based nanostructures demonstrated a remarkable photoluminescence (PL) signal (excited at 300 nm) that was more pronounced for the F+0.5 position. This laser ablation case led to better laser-induced heating of the colloidal solutions compared to samples prepared at other focus positions. All the formed silicon/gold nanocomposites demonstrated similar structures, regardless of laser ablation conditions. Our findings show the importance of attentive focusing of laser irradiation on the surface of the substrate, whose thickness decreases during prolonged treatment. To achieve reliable and reproducible high-quality results, the precision of focus should be regularly checked and adjusted depending on the thickness of the ablated targets.

2. Materials and Methods

Firstly, the precise position of the focus irradiation was estimated using a polished silicon wafer immersed in water (3 mm layer). For this purpose, we changed the wafer's position along the propagation of laser irradiation in the range of 5 mm, with a step of 0.1 mm, using a manually controlled mechanical translation stage (0.05 mm precision), and irradiated it with a single pulse (1030 nm, 6 ps, 25 μJ/pulse). We observed laser-ablated craters using an optical microscope (Figure 1) and analyzed their focus-dependent area. The crater with the minimum surface area corresponded to the exact position of focus.

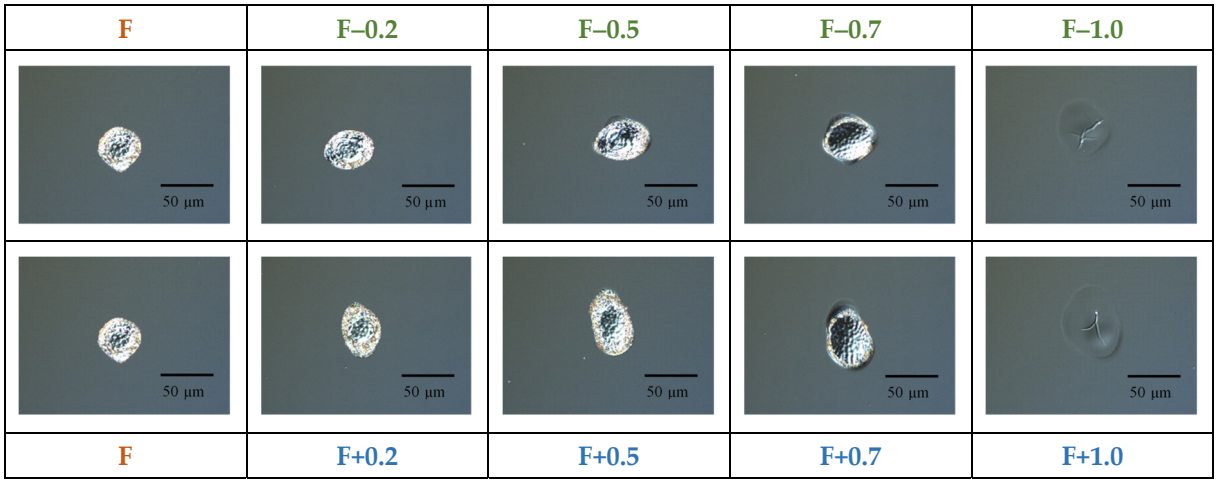

Figure 1. Optical microscope images of a silicon wafer irradiated with a single pulse at different positions of focus (1030 nm, 6 ps, 25 μJ/pulse, 1 pulse, 3 mm water level).

Afterwards, laser ablation synthesis of composite silicon/gold nanoparticles was carried out using the following two-step approaches. Firstly, either silicon or gold nanopar-

ticles were prepared by ablation of a silicon or a gold target, respectively, immersed in 10 mL of deionized water. The water level above the surface of the targets was 3 mm. The irradiation was performed by an infra-red laser with an ultra-short pulse duration (1030 nm, 6 ps, 25 μJ/pulse, 10 kHz). The ablation duration was 3 min. The laser beam was scanned across the surface using a Galvo scanner (10×10 mm^2 area). It was focused either exactly on the target surface (F), or 0.5 mm or 1 mm below it (F+0.5 and F+1.0, respectively). Secondly, the gold or silicon targets immersed in the previously prepared Si NP or Au NP colloidal solutions, respectively, were treated using the same experimental conditions. For clarity, these samples were named as Si-Au or Au-Si NPs, respectively.

The plasmonic properties of the synthesized nanostructures were investigated in the 300–800 nm spectral range by means of a UV-Vis spectrometer (Shimadzu 2700, Shimadzu Corporation, Kyoto, Japan) (2 nm slit width, 2 s accumulation time). Hydrodynamic diameter, chemical stability (ξ-potential), and particle concentration were obtained by means of multi-angle dynamic light scattering (MA-DLS) technique, using Malvern Ultra Size. To avoid distortions from highly concentrated NPs, all colloidal solutions were diluted 10-fold prior to the MA-DLS measurements. The electrical conductivity of the colloids was observed during ξ-potential measurements, and additionally controlled by a conductivity meter (Hanna PWT HI 98308) working in the 0–99.9 μS/cm range, with a 0.1 μS/cm precision (10 mm layer). Prior the measurements, correct conductivity values were checked using special calibration solutions.

The photoluminescence (PL) of the colloidal solutions was investigated using a spectrofluorometer (Edinburgh Instruments FLS1000), based on double-excitation and double-emission monochromators with customized focal distances (2×350 mm). Excitation of the samples was performed by a xenon lamp (350 W) at 300 nm and 350 nm. The emission signal was detected in the spectral range of 360–750 nm by a photo-multiplied tube (PMT) Hamamatsu PMT-R928P, cooled to −21 °C. Photoluminescence excitation (PLE) spectra were detected in the 230–410 nm excitation range at the 430 nm emission wavelength.

Heating of the colloidal solutions (1 mL in a plastic cuvette) was carried out by an infrared femtosecond laser (800 nm, 35 fs, 1 000 Hz) at 1.3 W average power. The temperature of the colloidal solutions was estimated by a thermal camera (Bosch GTC400C). The samples were irradiated for 7 min.

The structural properties of the nanostructures were analyzed by grazing incidence X-ray diffraction (GIXRD) for NPs coated on an amorphous SiO_2 substrate, using a Rigaku Smartlab X-ray diffractometer at a critical angle of ~0.3 degrees. Transmission electron microscopy (TEM) images were obtained using a Jeol JEM 3010 microscope.

Chemical composition was analyzed by inductively coupled plasma mass spectrometry (ICP-MS). A volume of 50 μL of each sample was decomposed in 3.0 mL of nitric acid (≥65% nitric acid, Analpure® grade from Analytika spol. s.r.o., Prague, Czech Republic) using a microwave-assisted digestion system (Speedwave 4, Berghof, Eningen unter Achalm, Germany). After digestion (10 min at 190 °C), the samples were diluted to 50 mL with ultrapure water (18.2 MΩ·cm, Millipore, Bedford, MA, USA), and analyzed by ICP-MS (NexION350D, Perkin-Elmer, Concord, ON, Canada). Calibration solutions of Cu and Zn, with concentrations ranging from 0 to 1 mg/L, were prepared using standard solutions from Analytika spol. s.r.o., Prague, Czech Republic (1000 ± 2 mg/L, Astasol®). Quantification was performed using external calibration.

3. Results and Discussion

In order to visualize the size and shape of craters under different experimental conditions, their optical microscopy images were recorded at various focus positions. The craters were formed due to a single ps pulse shot irradiation of a silicon wafer in water (Figure 1).

One can see the spherical crater with a diameter of approximately 30 μm. However, a slight deviation (0.5 mm) of the focus position along the axis perpendicular to the target surface led to remarkable change in the shape of the crater, affecting its dimensions. A further 0.5 mm shift (1.0 mm in total) resulted in the complete disappearance of the craters, showing just some damage area (Figure 1). Thus, exact focusing of laser irradiation on the target surface is considered to be a crucial parameter. The precision of the focus position can be affected by the target's thickness and the level of the liquid above the surface [36]. From this observation, the following focus positions were chosen for further experiments: exact focusing, named as "F"; and focusing located 0.5 mm and 1.0 mm below the target surface, named as "F+0.5" and "F+1.0". It is known that underwater material ablation by ultrafast laser pulses can lead to undesired nonlinear optical phenomena, e.g., water breakdown [37–39], which can additionally affect the properties of the synthesized nanostructures. In order to avoid such deviations, the focus was moved below the surface, rather than above it [39]. Typical TEM images of Si-Au and Au-Si NPs formed at the F focus position are presented in Figures 2a and 2b, respectively, showing nanostructures of similar shapes and dimensions (~15–20 nm mean size).

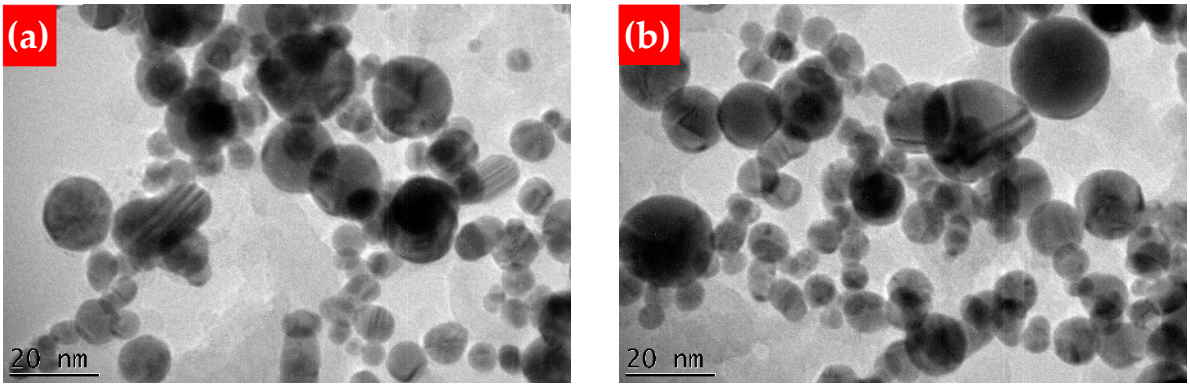

Figure 2. TEM images of Si-Au (**a**) and Au-Si NPs (**b**), prepared at the F focus position.

To reveal changes in the NP concentration, the latter was measured for both single- and double-element nanostructures at three different focus positions, using the DLS technique. One can see that the concentration of Si NPs was firstly increased 2.86-fold for the F+0.5 as compared to the F position, and decreased 1.7-fold for the F+1.0 position (Figure 3a). A similar behavior was also found for Au NPs: a 2.50-fold increase for the F+0.5 compared to the F position, and a 9.05-fold decrease for the F+1.0 position (Figure 3a). Such behavior can be due to a larger laser spot ablating a larger surface, while laser fluence is still greater than the ablation threshold. A similar situation was observed for both types of composite Si/Au NPs, but the concentration was approximately one order of magnitude greater for double- than for single-element nanostructures (Figure 3b). Higher concentrations can be caused by both (i) fragmentation of already existing NPs and (ii) ejection of other materials. Deepening the focus position led to a continuous increase in the hydrodynamic size of single-element NPs (Figure 3c). However, one can foresee here different reasons for these changes. The intermediate focus position (F+0.5) can increase hydrodynamic size due to a larger amount of ablated materials. Deeper focus (F+1.0) can result in the ejection of large clusters rather than of smaller nanoclusters, followed by their further aggregation. The larger size of Au NPs in comparison with Si NPs can be related to the different masses of these substances and, consequently, their different acquired kinetic energies (smaller for Au NPs). The continuous increase in the hydrodynamic size of composite NPs can be due to formation of shell levels from ablated materials on already-existing nanoparticles.

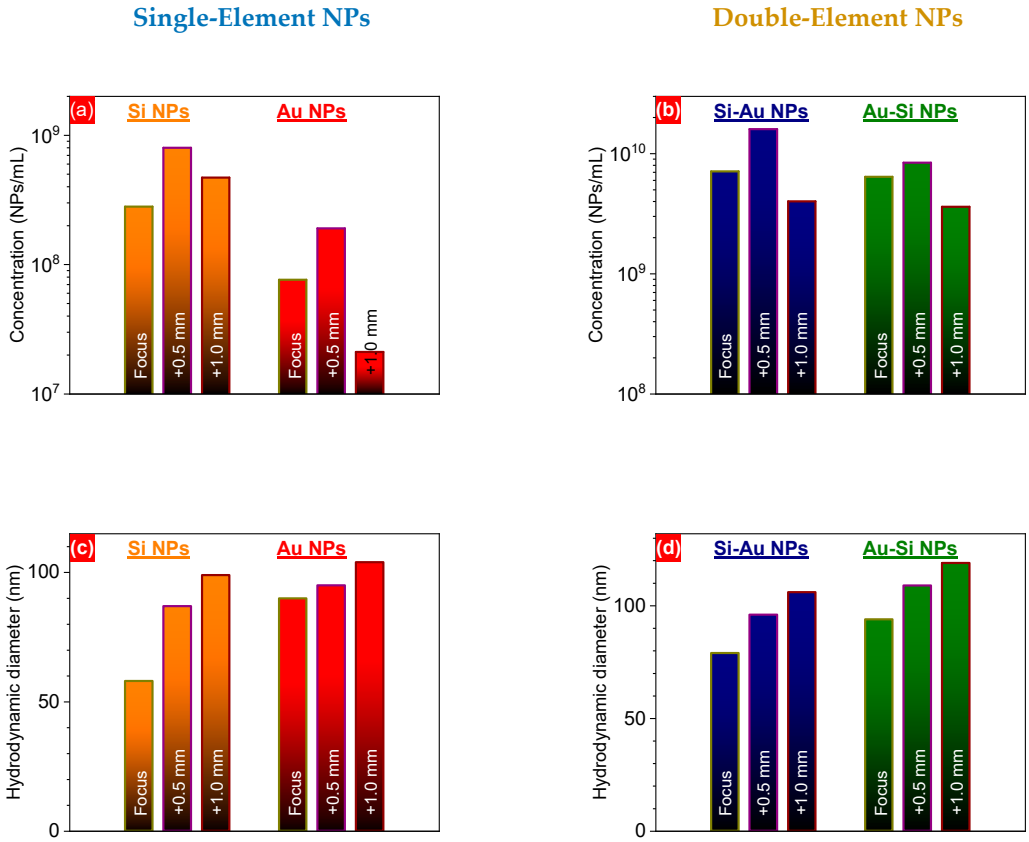

Figure 3. Nanoparticle concentrations (**a**,**b**) and hydrodynamic diameters (**c**,**d**) of one- (**a**,**c**) and two-component (**b**,**d**) NPs prepared by PLAL, at different focus positions.

Additionally, the mass concentration of different elements (silicon and gold) was measured by the ICP-MS technique (for Au), and by weighing the target before and after ablation (for Si). One can see that the F+0.5 focus position led to a higher concentration of silicon for both Si and Au-Si NPs, with a further decrease at the F+1.0 position (Table 1). This can be associated with the higher surface area of the F+0.5 position in comparison with the F one (Figure 1). The further decrease can be related to the significant modification of the laser irradiation spot, while the laser fluence can remain above the ablation threshold. The lower concentration of silicon in the Au-Si NPs compared to the pure Si NPs can be attributed to the much higher absorption of ps laser irradiation during the laser treatment. Although both Au NPs and Si NPs showed insignificant absorbance at ~1 µm (according to UV-Vis measurements), using ultrafast laser irradiation can lead to strong nonlinear effects that might exert considerable influence on the laser synthesis. Indeed, strong plasmonic absorption of Au-containing nanostructures with a ~520 nm peak can significantly reduce the laser energy of 1030 nm laser irradiation that is deposited on the target surface. A slight decrease in the silicon concentration of the Si-Au NPs in comparison with the Si NPs can be related to the stronger oxidation of silicon during the synthesis of composite nanostructures [15], accompanied by their further degradation. At the same time, the concentration of gold was similar in the case of Au NPs and Au-Si NPs (Table 1). Similarly to the silicon case, a deeper focus (F+0.5) resulted in a larger mass of ablated gold for both the Au and Au-Si NP samples. However, the F+1.0 position led to a mass of gold quite similar to that observed at the F+0.5 focus, which considerably differed from silicon. In this case, laser irradiation of the gold target at the F+1.0 position might eject large gold fragments, contrary to small nanoclusters in the previous cases. In the case of Si-Au NPs, the gold concentration was found to be similar, regardless of the focus position; this can be attributed to the attenuation of the laser energy due to light scattering by the Si NPs.

Table 1. Mass concentration (μg/mL) of silicon and gold elements in single- and double-element NPs, according to ICP-MS study.

		Silicon			Gold		
	Medium	**F**	**F+0.5**	**F+1.0**	**F**	**F+0.5**	**F+1.0**
Si	Water	50	63.5	25	-----	-----	-----
Si-Au	Si NPs	46.7	59.8	32.3	53.6	51.3	53.9
Au	Water	-----	-----	-----	58	78.7	73.5
Au-Si	Au NPs	28.6	57.1	28.6	56.8	79.8	74.8

The intermediate F+0.5 focus position led to a ~37% increase in the ξ-potential of single-element NPs, compared to the F position. Further deepening of focus inside the targets led to a considerable decrease in the potential (Figure 4a). A similar trend was also observed for both Si-Au and Au-Si NPs (Figure 4b). These variations can be mostly attributed to either the changes in the liquid medium used, or the nature of the nanoparticles [40,41]. Since deionized water was used for the synthesis of all nanoparticles, we can assume that the different structures and/or chemical compositions of the generated nanostructures are the most probable reasons for the ξ-potential variations. Therefore, one can expect a higher oxidation rate of Si and Au NPs in the case of the F+0.5 focus position, similar to the observed laser ablation time-dependent change in oxidation rate [15]. Indeed, a larger irradiation area can result in stronger interaction of ablated inorganic species with dissolved oxygen molecules. As a result of these photo-chemical reactions, oxygen can be incorporated into the core structure, leading to stronger oxidation of the nanostructures.

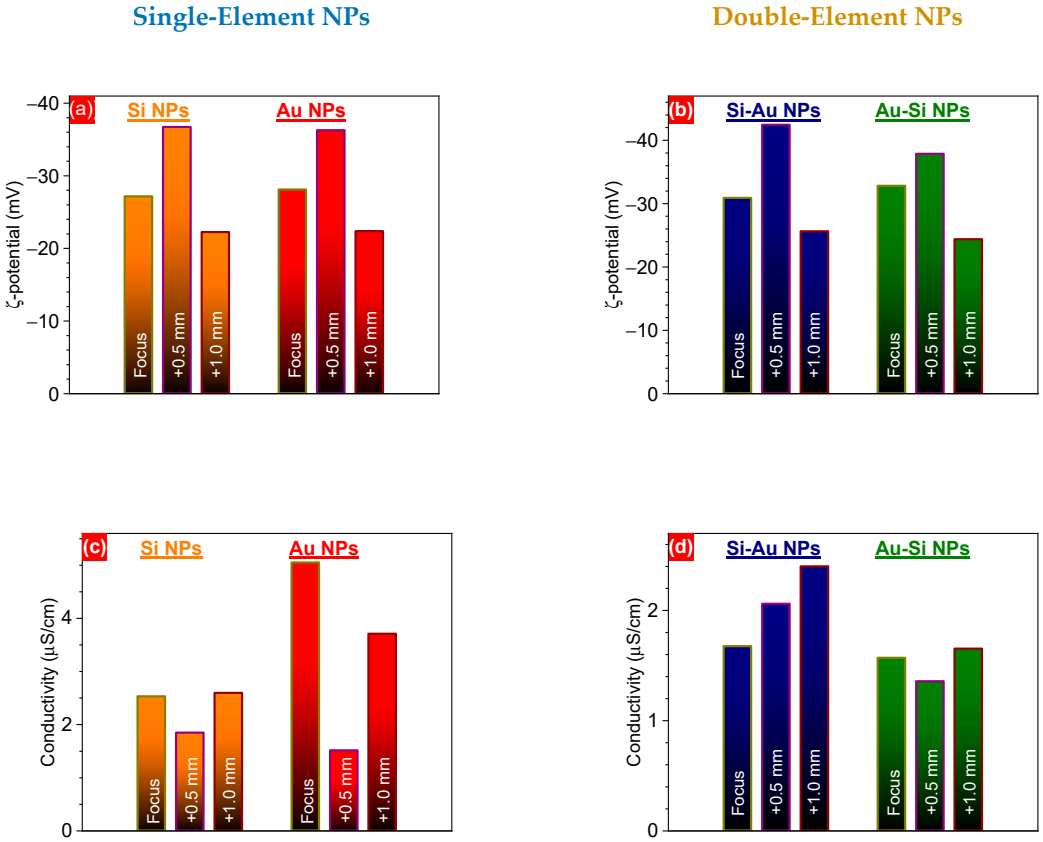

Figure 4. ξ-potential (**a**,**b**) and electrical conductivity (**c**,**d**) of one- (**a**,**c**) and two-component (**b**,**d**) NPs prepared by PLAL, at different focus positions.

A larger amount of oxygen atoms in the nanocomposites could also have led to the decreases in nanoparticle electrical conductivity that were observed experimentally (Figure 4c,d). The electrical conductivity value is associated with electron mobility, and is related to their mean free path. We expected that the focus position would strongly affect the conditions of agglomeration of nanoclusters and the growth of nanoparticles, due to changes in laser fluence. This can influence the interactions between silicon, gold, and oxygen atoms, leading to variation in the chemical composition of nanoparticles and the distribution of the elements within them. Moreover, it can also result in the growth of nanoparticles of different sizes, which can additionally affect the electrical conductivity values [42]. Moreover, we expected some changes in the surrounding liquid medium due to the possible degradation of nanoparticles. Indeed, as has been shown recently, more strongly oxidized Si NPs endure faster dissolution in an aqueous-based medium, due to the formation of charged complexes [19]. In turn, they can vary the pH of the solution, which strongly affects the ξ-potential of the dispersed nanoparticles [43]. In the case of composite nanostructures, some redistribution of charge carriers can take place, due to the laser-induced destruction of the initial nanomaterials and the further synthesis of composite ones. In order to clarify the mechanisms of these changes, a deeper study is required that considers the laser-assisted photo-chemical reactions, oxidation states (to be studied by XPS), and chemical compositions (to be studied by TEM-EDX) of nanoparticles, as well as their dissolution dynamics in aqueous media.

To reveal changes in absorbance efficiency, the optical properties of both single- (Figure 5a) and double-element (Figure 5b) NPs were observed for the nanostructures formed at different focus positions. One can see stronger absorbance by all the laser-synthesized NPs (e.g., ~29% for Au NPs and ~36% for Au-Si NPs at the plasmonic maximum) formed at the F+0.5 focus compared to the F one (Figure 5a,b). This correlates directly with the particle and mass concentrations of the nanostructures obtained by the DLS and ICP-MS methods, respectively. Further deepening of the focus position towards the F+1.0 position led to a decrease in the absorbance of all nanostructures (Figure 5a,b). It is known that absorbance efficiency is directly related to substance concentration [44], as shown in Equation (1).

$$A = \varepsilon \cdot b \cdot C \quad (1)$$

A—absorbance, ε—molar extinction coefficient, b—path length, C—concentration.

In addition, some slight shifts in the plasmonic maximum position of Au-based NPs can be associated with variations in the (i) size and (ii) chemical composition of the nanostructures, caused by modification of the focus position.

Thus, this correlates well with the concentration of silicon in the NPs prepared at the F+1.0 position, but contradicts the concentration of gold. As was suggested above, laser irradiation can lead to ejection of large aggregates, for instance, gold dimers, whose properties (e.g., molar extinction coefficient) can differ remarkably from small nanostructures. Indeed, it has been shown that the extinction coefficient of gold dimers significantly differs from that of individual NPs, depending on the size of nanoparticles and the distance between them [45]. Similar trends were found for the PLE spectra of Si- and/or Au-based laser-synthesized NPs detected at the 430 nm emission wavelength (Figure 5c,d). Some excitation peaks were observed at 300 nm and 350 nm for all types of NPs. However, one can observe a significant difference from the other spectra relating to two excitation bands at 250 nm and 310 nm for the Si NPs formed at the F+0.5 focus position. Considering the oxygen-related mechanisms of the PL [18], one can assume that there is much stronger interaction between silicon and oxygen molecules at the F+0.5 focus position, due to a larger irradiation cross-section. This can lead to stronger oxidation of Si NPs, which may

also have different sub-oxide forms. This hypothesis will be checked separately using X-ray photoelectron spectroscopy.

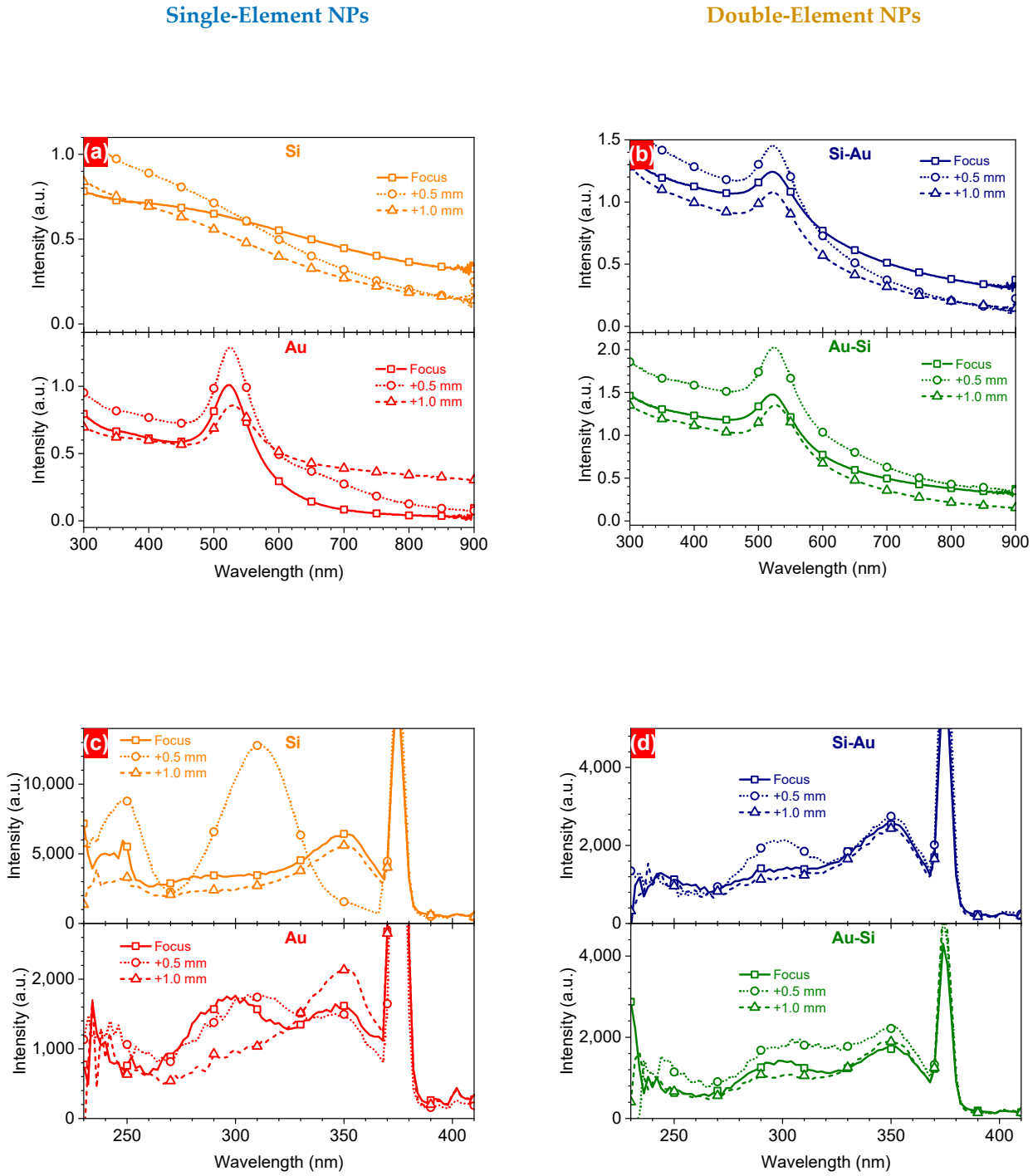

Figure 5. UV-Vis (**a**,**b**) and PLE (**c**,**d**) spectra of one- and two-component NPs prepared by PLAL, at different focus positions.

To check the emission properties of the colloidal solutions of the laser-generated NPs, they were excited at 300 nm and 350 nm by a xenon lamp via an excitation monochromator. One can see remarkable responses for all Si-containing nanostructures, with some spectral features for Au NPs (Figure 6a,b). In all cases, the PL spectra observed for the NPs formed at the F+0.5 focus position showed stronger emission compared to the F position. This directly correlates with the better excitation efficiencies (Figure 5c,d) of the NPs, which can be caused by a higher concentration of the material. Moreover, Si NPs prepared at the

F+0.5 focus exhibited quite a strong PL signal at ~430 nm, correlating with the effective PLE. However, excitation at 350 nm showed just some features in this region, accompanied by a strong Raman signal from surrounding water. Changes in the position of the emission bands can be associated with the formation of gold acceptors ($E_C - 0.55$ eV) and donors ($E_V + 0.35$ eV) in the silicon band gap with different densities of states, which could have led to the observed changes [18].

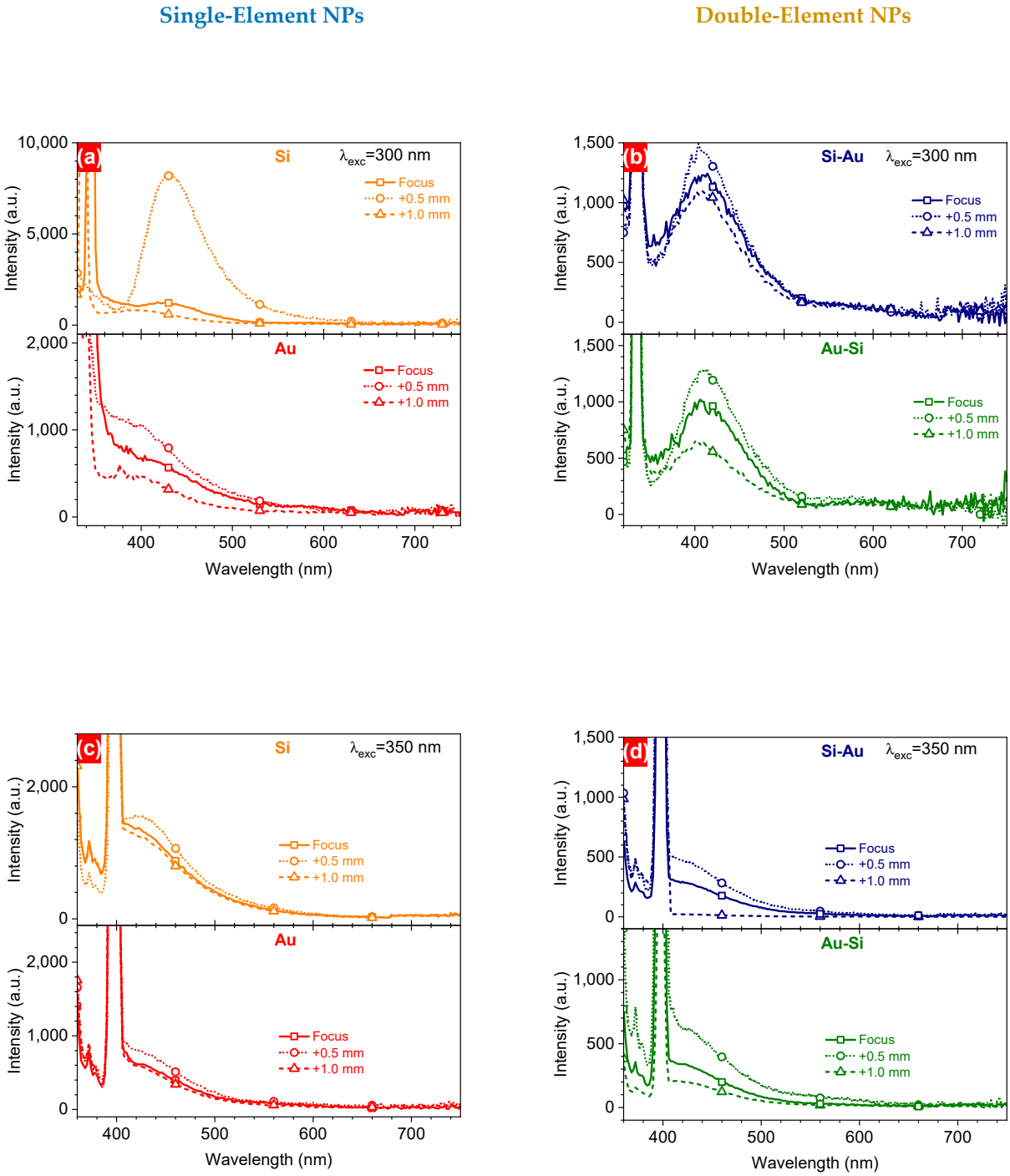

Figure 6. PL spectra of one- (**a**,**c**) and two-component (**b**,**d**) NPs prepared by PLAL at different focus positions, excited at 300 nm (**a**,**b**) and 350 nm (**c**,**d**).

To assess the impact of the focus position on the efficiency of the laser-induced heating of the colloidal solutions, they were irradiated with an unfocused beam for 7 min. For this purpose, the laser beam was centered in the middle of the studied solution volume (y and z

axes) and propagated through the liquid along the *x*-axis (Figure 7). Before irradiation, all solutions were stabilized at room temperature for at least 2 h, to bring them to an initial temperature of 23 °C. Laser radiation propagated through the samples was absorbed by the dispersed nanoparticles with further conversion into heat, which can further be used for theranostic applications [21]. As a result, all the samples demonstrated a remarkable heating of the solutions, depending on the chemical composition of the nanostructures (Figure 7). In the majority of cases, the NPs formed at the F+0.5 focus position demonstrated better heating efficiency, reaching a value of ~0.80–0.85 °C/min, contrary to those prepared at the F position (Figure 8). This fact can be associated with higher material concentrations, as was shown above:

- 59.8 μg/mL of Si and 51.3 μg/mL of Au for Si-Au NPs;
- 57.1 μg/mL of Si and 79.8 μg/mL of Au for Au-Si NPs.

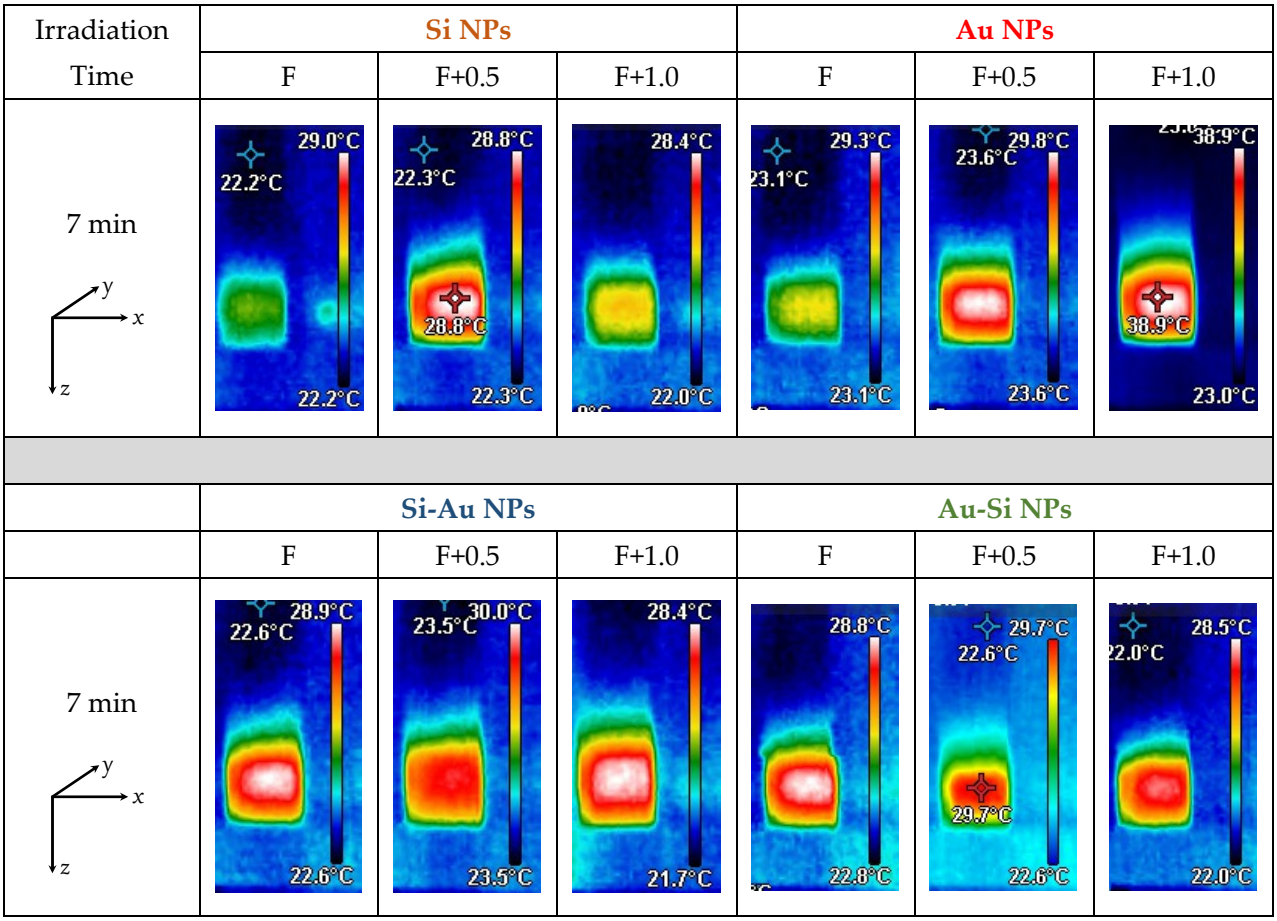

Figure 7. Images of fs laser-induced heating of colloidal solutions of single- and double-element NPs, at 7 min of fs laser irradiation.

The laser-induced heating efficiency was comparable to that previously reported for Au-SiC NPs (~0.85 °C/min) prepared and irradiated under similar conditions, but almost two times less than that of Au-Ge nanocomposites [19]. A comparable heating efficiency (~0.8 °C/min) was also achieved for laser-ablated colloidal solutions of C-Au and C-Ag nanocomposites [16].

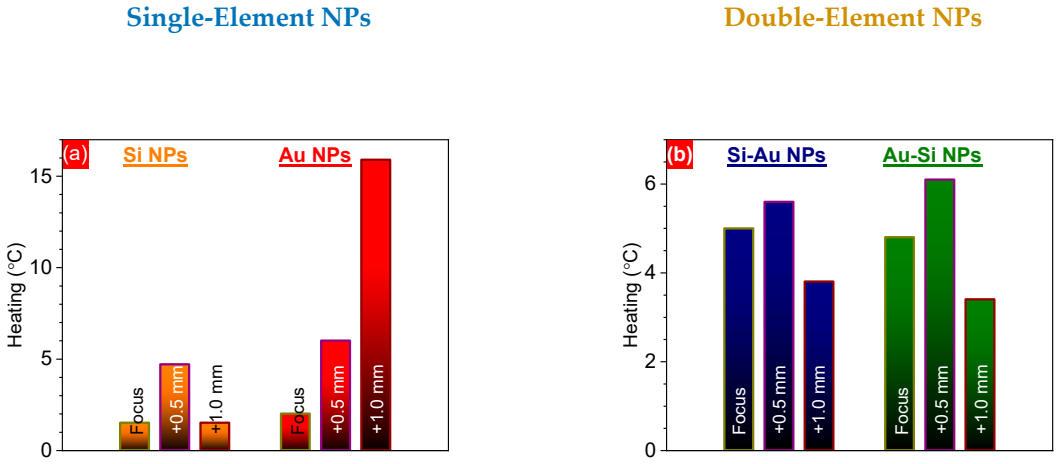

Figure 8. Heating temperatures of one- (**a**) and two-component (**b**) NPs prepared by PLAL at F, F+0.5, and F+1.0 focus positions, affected by fs laser irradiation.

The better heating efficiency of the plasmonic nanostructures can be attributed to the much lower values of the specific heat capacity of gold {~121 J/(kg·K)} in comparison with Si {~710 J/(kg·K)} [46]. The considerably stronger heating of the Au NPs formed at the F+1.0 position might be related to gold aggregates/dimers having a higher material concentration. Indeed, a system containing dimers of Au NPs demonstrated considerably higher field enhancement compared to similar monomer systems (~5-fold for 100 nm Au NPs, with a 10 nm gap for a dimer) [47]. This led to a ~7-fold larger absorption cross-section of 800 nm of fs laser irradiation by Au NPs dimers in comparison with monomers, which could have caused the observed 8-fold stronger heating of NPs formed at the F+1.0 position (Figure 8a). To check the structure of the composite NPs formed at the different focus positions, the nanostructures deposited on a carbon tape were analyzed using the grazing incidence X-ray diffraction (GIXRD) technique (Figure 9). One can see that the GIXRD patterns were very similar for both the Si-Au and Au-Si NPs formed at the three different focus positions, being independent of these (Figure 9). Some weak reflexes can be assigned to the (111) crystalline planes of silicon (28°) and gold (38°) [48,49]. In addition, some intensive reflexes in the 21–23° range were observed, that can be related to the different crystalline planes of gold silicide phases of different stoichiometry (e.g., Au_3Si (200) at 22.7° [50]). Moreover, the strong background in the range of 20–28° is related to amorphous silicon [51], suggesting strong silicon oxidation in the aqueous atmosphere. The presence of amorphous and oxidation states of nanocomposites have been previously confirmed by EPR and XPS methods, respectively [12,15]. Surprisingly, the nanocomposite structure in this study was different from that of previously prepared silicon–gold nanostructures [15]. Here, the different laser fluences used for the NP synthesis can be identified as the most relevant reasons for the observed changes. Indeed, a lower laser energy deposited on the target surface can lead to a lower amount of gold nanoclusters, as was confirmed by the ICP-MS study [15]. Moreover, a lower energy value might also be very crucial, being very close to the ablation threshold of gold. Indeed, the estimated ablation thresholds for Au and Si in water at 6 ps are ~1.3 J/cm^2 and ~3.0 J/cm^2 [52,53]. At the same time, the calculated laser fluence in the current case was ~ 3.2 J/cm^2. Thus, another regime of laser ablation/decomposition of gold can occur while using 25 μJ/pulse laser fluence. Hence, the formation of composite NPs should be additionally studied at various laser energies near the gold ablation threshold in water, in order to reveal the structural changes in composite silicon/gold nanostructures. The achieved findings demonstrate no impacts of the focus position of laser irradiation on the structural properties of silicon/gold nanostructures,

while their concentration and optical properties were found to be the most effective at the focus position located 0.5 mm below the water/surface interface.

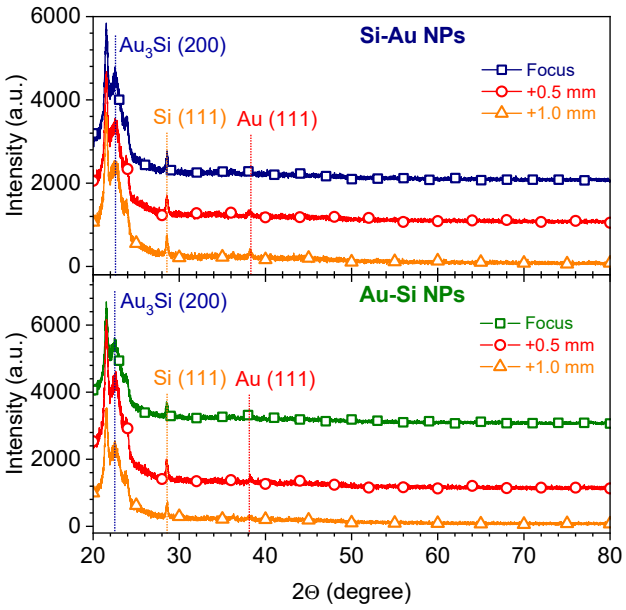

Figure 9. GIXRD patterns of two-component Si/Au NPs prepared by PLAL at different focus positions.

4. Conclusions

In summary, single- and double-element silicon/gold nanoparticles were produced by ps laser ablation in water using different focus positions. The best position was obtained for the focus located 0.5 mm below the surface of the targets. This resulted in better chemical stability of the synthesized nanoparticles, accompanied by less electrical conductivity. It also led to stronger light absorption by all the synthesized nanostructures, due to higher nanomaterial concentration, provoking better efficiency of both PLE and PL signals. Moreover, stronger fs laser-induced heating of the colloidal solutions was also achieved at this irradiation condition for the majority of nanostructures. These findings contribute to the field of pulsed laser ablation in liquids by suggesting more careful controlling of irradiation conditions in order to achieve more reliable and repeatable data for different semiconductor–metallic nanostructures.

Author Contributions: Y.V.R. designed the research and performed the validation. Y.V.R. performed the TEM, UV-Vis, DLS, PL, and laser-induced heating experiments, and analyzed the corresponding experimental data. I.M. performed the XRD and laser-induced heating experiments, and analyzed the corresponding experimental data. A.K. performed the ICP-MS experiments, and analyzed the corresponding experimental data. All authors wrote and reviewed the manuscript and agreed with the final version of the manuscript. All authors have read and agreed to the published version of the manuscript.

Funding: This research was funded by the Czech MEYS and the European Regional Development Fund (Project No. SenDiSo—CZ.02.01.01/00/22_008/0004596), and by the European Union's Horizon 2020 research and innovation programme (grant agreement No. 897231, LaDeNTher).

Data Availability Statement: The original data presented in the study are openly available in https://doi.org/10.57680/asep.0604558, accessed on 14 January 2025.

Conflicts of Interest: The authors declare no conflicts of interest.

References

1. Zhang, D.; Gökce, B.; Barcikowski, S. Laser Synthesis and Processing of Colloids: Fundamentals and Applications. *Chem. Rev.* **2017**, *117*, 3990–4103. [CrossRef]
2. Zhang, D.; Li, Z.; Sugioka, K. Laser ablation in liquids for nanomaterial synthesis: Diversities of targets and liquids. *J. Phys. Photonics* **2021**, *3*, 042002. [CrossRef]
3. Amendola, V.; Meneghetti, M. What controls the composition and the structure of nanomaterials generated by laser ablation in liquid solution? *Phys. Chem. Chem. Phys.* **2013**, *15*, 3027–3046. [CrossRef] [PubMed]
4. Kanitz, A.; Kalus, M.-R.; Gurevich, E.L.; Ostendorf, A.; Barcikowski, S.; Amans, D. Review on experimental and theoretical investigations of the early stage, femtoseconds to microseconds processes during laser ablation in liquid-phase for the synthesis of colloidal nanoparticles. *Plasma Sources Sci. Technol.* **2019**, *28*, 103001. [CrossRef]
5. Nichols, W.T.; Sasaki, T.; Koshizaki, N. Laser ablation of a platinum target in water. II. Ablation rate and nanoparticle size distributions. *J. Appl. Phys.* **2006**, *100*, 114912. [CrossRef]
6. Moura, C.G.; Pereira, R.S.F.; Andritschky, M.; Lopes, A.L.B.; Grilo, J.P.F.; Nascimento, R.M.; Silva, F.S. Effects of laser fluence and liquid media on preparation of small Ag nanoparticles by laser ablation in liquid. *Opt. Laser Technol.* **2017**, *97*, 20–28. [CrossRef]
7. Tsuji, T.; Iryo, K.; Watanabe, N.; Tsuji, M. Preparation of silver nanoparticles by laser ablation in solution: Influence of laser wavelength on particle size. *Appl. Surf. Sci.* **2002**, *202*, 80–85. [CrossRef]
8. Tsuji, T.; Iryo, K.; Nishimura, Y.; Tsuji, M. Preparation of metal colloids by a laser ablation technique in solution: Influence of laser wavelength on the ablation efficiency (II). *J. Photochem. Photobiol. A* **2001**, *145*, 201–207. [CrossRef]
9. Elsayed, K.A.; Imam, H.; Ahmed, M.A.; Ramadan, R. Effect of focusing conditions and laser parameters on the fabrication of gold nanoparticles via laser ablation in liquid. *Opt. Laser Technol.* **2013**, *45*, 495–502. [CrossRef]
10. Dittrich, S.; Streubel, R.; McDonnell, C.; Huber, H.P.; Barcikowski, S.; Gökce, B. Comparison of the productivity and ablation efficiency of different laser classes for laser ablation of gold in water and air. *Appl. Phys. A* **2019**, *125*, 432. [CrossRef]
11. Attallah, A.H.; Abdulwahid, F.S.; Ali, Y.A.; Haider, A.J. Effect of Liquid and Laser Parameters on Fabrication of Nanoparticles via Pulsed Laser Ablation in Liquid with Their Applications: A Review. *Plasmonics* **2023**, *18*, 1307–1323. [CrossRef]
12. Flimelová, M.; Ryabchikov, Y.V.; Behrends, J.; Bulgakova, N.M. Environmentally Friendly Improvement of Plasmonic Nanostructure Functionality towards Magnetic Resonance Applications. *Nanomaterials* **2023**, *13*, 764. [CrossRef]
13. Mahdieh, M.H.; Fattahi, B. Size properties of colloidal nanoparticles produced by nanosecond pulsed laser ablation and studying the effects of liquid medium and laser fluence. *Appl. Surf. Sci.* **2015**, *329*, 47–57. [CrossRef]
14. Menéndez-Manjón, A.; Barcikowski, S. Hydrodynamic size distribution of gold nanoparticles controlled by repetition rate during pulsed laser ablation in water. *Appl. Surf. Sci.* **2011**, *257*, 4285–4290. [CrossRef]
15. Ryabchikov, Y.V.; Mirza, I.; Flimelová, M.; Kana, A.; Romanyuk, O. Merging of Bi-Modality of Ultrafast Laser Processing: Heating of Si/Au Nanocomposite Solutions with Controlled Chemical Content. *Nanomaterials* **2024**, *14*, 321. [CrossRef]
16. Ryabchikov, Y.V.; Zaderko, A. "Green" Fluorescent–Plasmonic Carbon-Based Nanocomposites with Controlled Performance for Mild Laser Hyperthermia. *Photonics* **2023**, *10*, 1229. [CrossRef]
17. Ryabchikov, Y.V. Size Modification of Optically Active Contamination-Free Silicon Nanoparticles with Paramagnetic Defects by Their Fast Synthesis and Dissolution. *Phys. Status Solidi* **2019**, *216*, A1800685. [CrossRef]
18. Ryabchikov, Y.V. Design of "green" plasmonic nanocomposites with multi-band blue emission for ultrafast laser hyperthermia. *Nanoscale* **2024**, *16*, 19453–19468. [CrossRef] [PubMed]
19. Yu, V. Facile Laser Synthesis of Multimodal Composite Silicon/Gold Nanoparticles with Variable Chemical Composition. *J. Nanopart. Res.* **2019**, *21*, 85. [CrossRef]
20. Saraeva, I.N.; Luong, N.V.; Kudryashov, S.I.; Rudenko, A.A.; Khmelnitskiy, R.A.; Shakhmin, A.L.; Kharin, A.Y.; Ionin, A.A.; Zayarny, D.A.; Tung, D.H.; et al. Laser synthesis of colloidal Si@Au and Si@Ag nanoparticles in water via plasma-assisted reduction. *J. Photochem. Photobiol. A* **2018**, *360*, 125–131. [CrossRef]
21. Gurbatov, S.O.; Zhizhchenko, A.Y.; Nesterov, V.Y.; Modin, E.B.; Zabotnov, S.V.; Kuchmizhak, A.A. Au–Si Nanocomposites with High Near-IR Light-to-Heat Conversion Efficiency via Single-Step Reactive Laser Ablation of Porous Silicon for Theranostic Applications. *ACS Appl. Nano Mater.* **2024**, *7*, 10779–10786. [CrossRef]
22. Elsayed, K.A.; Alomari, M.; Drmosh, Q.A.; Manda, A.A.; Haladu, S.A.; Alade, I.O. Anticancer Activity of TiO_2/Au Nanocomposite Prepared by Laser Ablation Technique on Breast and Cervical Cancers. *Opt. Laser Technol.* **2022**, *149*, 107828. [CrossRef]
23. Gurbatov, S.O.; Modin, E.; Puzikov, V.; Tonkaev, P.; Storozhenko, D.; Sergeev, A.; Mintcheva, N.; Yamaguchi, S.; Tarasenka, N.N.; Chuvilin, A.; et al. Black Au-Decorated TiO_2 Produced via Laser Ablation in Liquid. *ACS Appl. Mater. Interfaces* **2021**, *13*, 6522–6531. [CrossRef] [PubMed]
24. Besner, S.; Kabashin, A.V.; Winnik, F.M.; Meunier, M. Synthesis of Size-Tunable Polymer-Protected Gold Nanoparticles by Femtosecond Laser-Based Ablation and Seed Growth. *J. Phys. Chem. C* **2009**, *113*, 9526–9531. [CrossRef]
25. Baladi, A.; Mamoor, R.S. Investigation of different liquid media and ablation times on pulsed laser ablation synthesis of aluminum nanoparticles. *Appl. Surf. Sci.* **2010**, *256*, 7559–7564. [CrossRef]

26. Ouyang, P.; Li, P.; Leksina, E.G.; Michurin, S.V.; He, L. Effect of liquid properties on laser ablation of aluminum and titanium alloys. *Appl. Surf. Sci.* **2016**, *360*, 880–888. [CrossRef]
27. Bajaj, G.; Soni, R.K. Effect of liquid medium on size and shape of nanoparticles prepared by pulsed laser ablation of tin. *Appl. Phys. A* **2009**, *97*, 481–487. [CrossRef]
28. Sylvestre, J.-P.; Kabashin, A.V.; Sacher, E.; Meunier, M. Femtosecond laser ablation of gold in water: Influence of the laser-produced plasma on the nanoparticle size distribution. *Appl. Phys. A* **2005**, *80*, 753–758. [CrossRef]
29. Barcikowski, S.; Menéndez-Manjón, A.; Chichkov, B.; Brikas, M.; Račiukaitis, G. Generation of nanoparticle colloids by picosecond and femtosecond laser ablations in liquid flow. *Appl. Phys. Lett.* **2007**, *91*, 083113. [CrossRef]
30. Nastulyavichus, A.; Kudryashov, S.; Ionin, A.; Yushina, Y.; Semenova, A.; Gonchukov, S. Focusing effects during ultrashort-pulse laser ablative generation of colloidal nanoparticles for antibacterial applications. *Laser Phys. Lett.* **2022**, *19*, 065601. [CrossRef]
31. Stasic, J.; Joksic, G.; Zivkovic, L.; Mihailescu, I.N.; Ghica, C.; Kuncser, A.; Trtica, M. Focusing geometry-induced size tailoring of silver nanoparticles obtained by laser ablation in water. *Laser Phys.* **2014**, *24*, 106005. [CrossRef]
32. Yang, Y.; Zhang, M.; Song, H.; Yu, C. Silica-Based Nanoparticles for Biomedical Applications: From Nanocarriers to Biomodulators. *Acc. Chem. Res.* **2020**, *53*, 1545–1556. [CrossRef]
33. Ryabchikov, Y.V.; Belogorokhov, I.A.; Gongalskiy, M.B.; Osminkina, L.A.; Timoshenko, V.Y. Photosensitized Generation of Singlet Oxygen in Powders and Aqueous Suspensions of Silicon Nanocrystals. *Semiconductors* **2011**, *45*, 1059–1063. [CrossRef]
34. Anik, M.I.; Mahmud, N.; Masud, A.A.; Hasan, M. Gold nanoparticles (GNPs) in biomedical and clinical applications: A review. *Nano Select* **2022**, *3*, 792–828. [CrossRef]
35. Sarfraz, N.; Khan, I. Plasmonic Gold Nanoparticles (AuNPs): Properties, Synthesis and their Advanced Energy, Environmental and Biomedical Applications. *Chem. Asian J.* **2021**, *16*, 720–742. [CrossRef]
36. Mahdieh, M.H.; Fattahi, B. Effects of water depth and laser pulse numbers on size properties of colloidal nanoparticles prepared by nanosecond pulsed laser ablation in liquid. *Opt. Laser Technol.* **2015**, *75*, 188–196. [CrossRef]
37. Zheng, C.; Shen, H. Understanding nonlinear optical phenomenon for underwater material ablation by ultrafast laser with high pulse energy. *J. Manuf. Process.* **2021**, *70*, 331–340. [CrossRef]
38. Feng, Q.; Moloney, J.V.; Newell, A.C.; Wright, E.M.; Cook, K.; Kennedy, P.K.; Hammer, D.X.; Rockwell, B.A.; Thompson, C.R. Theory and simulation on the threshold of water breakdown induced by focused ultrashort laser pulses. *IEEE J. Quantum Elect.* **1997**, *33*, 127–137. [CrossRef]
39. Kanitz, A.; Hoppius, J.S.; Fiebrandt, M.; Awakowicz, P.; Esen, C.; Ostendorf, A.; Gurevich, E.L. Impact of liquid environment on femtosecond laser ablation. *Appl. Phys. A* **2017**, *123*, 674. [CrossRef]
40. Pochapski, D.J.; Santos, C.C.D.; Leite, G.W.; Pulcinelli, S.H.; Santilli, C.V. Zeta Potential and Colloidal Stability Predictions for Inorganic Nanoparticle Dispersions: Effects of Experimental Conditions and Electrokinetic Models on the Interpretation of Results. *Langmuir* **2021**, *37*, 13379–13389. [CrossRef]
41. Lowry, G.V.; Hill, R.J.; Harper, S.; Rawle, A.F.; Hendren, C.O.; Klaessig, F.; Nobbmann, U.; Sayre, P.; Rumble, J. Guidance to improve the scientific value of zeta-potential measurements in nanoEHS. *Environ. Sci. Nano* **2016**, *3*, 953–965. [CrossRef]
42. Abdelhalim, M.A.K.; Mady, M.M.; Ghannam, M.M. Dielectric constant, electrical conductivity and relaxation time measurements of different gold nanoparticle sizes. *Int. J. Phys. Sci.* **2011**, *6*, 5487–5491. [CrossRef]
43. Berg, J.M.; Romoser, A.; Banerjee, N.; Zebda, R.; Sayes, C.M. The relationship between pH and zeta potential of ∼30 nm metal oxide nanoparticle suspensions relevant to in vitro toxicological evaluations. *Nanotoxicology* **2009**, *3*, 276–283. [CrossRef]
44. Lodeiro, P.; Achterberg, E.P.; El-Shahawi, M.S. Detection of silver nanoparticles in seawater at ppb levels using UV–visible spectrophotometry with long path cells. *Talanta* **2017**, *164*, 257–260. [CrossRef]
45. Dolinnyi, A.I. Extinction Coefficients of Gold Nanoparticles and Their Dimers. Dependence of Optical Factor on Particle Size. *Colloid J.* **2017**, *79*, 611–620. [CrossRef]
46. Available online: https://periodictable.com/Properties/A/SpecificHeat.an.html (accessed on 24 January 2025).
47. Hatef, A.; Meunier, M. Plasma-mediated photothermal effects in ultrafast laser irradiation of gold nanoparticle dimers in water. *Optics Express* **2015**, *23*, 1967–1980. [CrossRef]
48. Daulay, A.; Gea, A.M.S. Synthesis Si nanoparticles from rice husk as material active electrode on secondary cell battery with X-Ray diffraction analysis. *S. Afr. J. Chem. Eng.* **2022**, *42*, 32–41. [CrossRef]
49. Juraić, K.; Gracin, D.; Djerdj, I.; Lausi, A.; Čeh, M.; Balzar, D. Structural analysis of amorphous-nanocrystalline silicon thin films by grazing incidence X-ray diffraction. *Nucl. Instrum. Methods Phys. Res. Sect. B Beam Interact. Mater. At.* **2012**, *284*, 78–82. [CrossRef]
50. Chang, J.F.; Young, T.F.; Yang, Y.L.; Ueng, H.Y.; Chang, T.C. Silicide formation of Au thin films on (1 0 0) Si during annealing. *Mater. Chem. Phys.* **2004**, *83*, 199–203. [CrossRef]
51. Shabir, Q.; Pokale, A.; Loni, A.; Johnson, D.R.; Fenollosa, R.; Tymczenko, M.; Rodríguez, I.; Meseguer, F.; Cros, A.; Cantarero, A. Medically Biodegradable Hydrogenated Amorphous Silicon Microspheres. *Silicon* **2011**, *3*, 173–176. [CrossRef]

52. Saraeva, I.N.; Kudryashov, S.I.; Rudenko, A.A.; Zhilnikova, M.I.; Ivanov, D.S.; Zayarny, D.A.; Simakin, A.V.; Ionin, A.A.; Garcia, M.E. Effect of fs/ps laser pulsewidth on ablation of metals and silicon in air and liquids, and on their nanoparticle yields. *Appl. Surf. Sci.* **2019**, *470*, 1018–1034. [CrossRef]
53. Spellauge, M.; Doñate-Buendía, C.; Barcikowski, S.; Gökce, B.; Huber, H.P. Comparison of ultrashort pulse ablation of gold in air and water by time-resolved experiments. *Light Sci. Appl.* **2022**, *11*, 68. [CrossRef]

Disclaimer/Publisher's Note: The statements, opinions and data contained in all publications are solely those of the individual author(s) and contributor(s) and not of MDPI and/or the editor(s). MDPI and/or the editor(s) disclaim responsibility for any injury to people or property resulting from any ideas, methods, instructions or products referred to in the content.